A Compact, Reconfigurable, Multi-UWB Radar for Snow Thickness Evaluation and Altimetry: Development and Field Trials

Fernando Rodríguez-Morales, *Senior Member, IEEE*, Jilu Li, *Senior Member, IEEE*, Daniel Gomez-García Alvestegui, *Member, IEEE*, Jiaxuan Shang, Emily J. Arnold, *Member, IEEE*, Carlton J. Leuschen, *Member, IEEE*, Christopher F. Larsen, Andrew Shepherd, Sine Munk Hvidegaard, and René Forsberg

***Abstract*—We developed a portable ultra-wideband radar system capable of reconfigurable operation in multiple frequency bands (separate or simultaneous) spanning from microwaves through millimeter waves. The instrument provides a compact solution for fine-resolution measurements of elevation changes and superficial snow/firn thickness from low-altitude, mid-sized airborne platforms. In this article, we provide an overview of the radar system design and its performance during laboratory testing. We demonstrate its application in aerial surveys of snow layer thickness at S/C bands, dual-band airborne altimetry at *Ku*-/*Ka*-bands, and present first-order comparisons with coincident airborne lidar data.**

***Index Terms*—Multiband altimeter, multi-ultra-wideband (UWB) radar, snow-probing radar.**

I. Introduction

AIRBORNE radar systems operating at microwave and millimeter-wave frequencies are a key technology for wide-area determination of snow cover thickness, ice-sheet firn density, and superficial topography variations in cold regions. By exploiting differences in signal penetration depths and backscattering signatures at different bands, these systems can accommodate diverse measurement scenarios to capture spatial and temporal changes of snow cover properties [1]–[8].

Airborne radars are also an invaluable tool for the validation of existing satellite data and for the exploration of future orbital mission concepts [9]. For example, the upcoming Copernicus Polar Ice and Snow Topography Altimeter mission is aimed at providing sea ice thickness retrievals and monitoring ice-sheet surface changes from space [10]. The mission will carry out coincident radar measurements at *Ku*- and *Ka*-bands to provide improved spatio-temporal resolution for the monthly quantification of sea ice thickness [11]; and for firn density estimates, which are needed for ice sheet mass-balance assessment and prognosis [12].

Satellite-based measurements require validation and ground truth verification via *in situ* and airborne sensor investigations, which can provide an independent assessment of snow thickness as well as surface and subsurface conditions. Multiband radars with ultra-wideband (UWB) capabilities can offer complementary altimetry information with much finer spatial resolution than spaceborne measurements and wider coverage with respect to *in situ* observations. Moreover, broadband data from these radars can be used "as is" to yield cm-scale vertical resolution; or can be spectrally segmented to emulate the operating parameters of spaceborne sensors.

The use of multiband radar systems for snow studies has been demonstrated extensively using ground-based equipment [13]–[17]. In contrast, the operation of multi-UWB airborne radars requires submillisecond sweeps, higher pulse repetition frequencies, and increased data rates. These features became realizable as technology advanced in recent years. Currently, the operation of high-performance aerial radar systems for snow studies involves the following main scenarios.

1) Separate large- and mid-size systems operating onboard platforms with moderate restrictions on payload size, weight, and power [18]–[21].
2) Separate single-band compact instruments for operation on manned or unmanned vehicles [2], [22]–[27].
3) Inherently multiband systems with relatively narrow-band capabilities [28], [29].

We developed a compact, nadir-looking multi-UWB radar system with the remarkable capability of collecting data with up

Manuscript received February 28, 2021; revised May 22, 2021; accepted June 8, 2021. Date of publication June 24, 2021; date of current version July 14, 2021. This work was supported in part by the U.S. National Aeronautics and Space Administration under Grant NNX10AT68G, in part by the National Oceanic and Atmospheric Administration under Grant NA19OAR4590206, in part by the U.K. Natural Environment Research Council under Grant NE/J005681/1, and in part by the European Space Agency CryoVex Campaign under Contract 4000128488/19/NL/FF/gp. *(Corresponding author: Fernando Rodríguez-Morales.)*

Fernando Rodríguez-Morales, Jilu Li, Daniel Gomez-García Alvestegui, Jiaxuan Shang, Emily J. Arnold, and Carlton J. Leuschen are with the Center for Remote Sensing of Ice Sheets, University of Kansas, Lawrence, KS 66045 USA (e-mail: frodrigu@ku.edu; jiluli@ku.edu; dgomezgarcia@ku.edu; jiaxuan.shang@ku.edu; earnold@ku.edu; leuschen@ku.edu).

Christopher F. Larsen is with the University of Alaska Fairbanks, Fairbanks, AK 99775 USA (e-mail: cflarsen@alaska.edu).

Andrew Shepherd is with the NERC Centre for Polar Observation and Modelling, University of Leeds, Leeds LS2 9JT, U.K. (e-mail: a.shepherd@leeds.ac.uk).

Sine Munk Hvidegaard and René Forsberg are with the National Space Institute, Technical University of Denmark, 2800 Kongens Lyngby, Denmark (e-mail: smh@space.dtu.dk; rf@space.dtu.dk).

Digital Object Identifier 10.1109/JSTARS.2021.3092313

to ∼18 GHz cumulative bandwidth, distributed in three separate bands: S/C (2–8 GHz), *Ku* (12–18 GHz), and *Ka* (32–38 GHz). The system's small form factor and relative low power consumption make it easy to integrate and operate onboard mid-size aircraft, which are well suited for low-altitude surveys [<1000 m above ground level (AGL)] in cold regions. The sensitivity and vertical resolution of this system across its operating bands is comparable to that of the three separate instruments flown on larger aircraft as a part of NASA Operation IceBridge (OIB) between 2009 and 2016 [30].

As an extension of our work in [31]–[33], here we provide relevant design aspects and show how the configurability of the instrument is advantageous to support various platforms and measurement scenarios. For example, we have used it to perform measurements of snow cover [31] and forest canopy [33] in Alaska onboard a Single Otter airplane; dual-band *Ku/Ka* altimetry measurements in the Arctic onboard a Twin Otter [32]; firn measurements at *Ku*-/*Ka*-bands in Greenland using a surface-based setup; and terrestrial snow measurements in the continental USA onboard a Cessna 172. The primary additions of this article with respect to previous publications [31]–[33] include the following. First, we provide details regarding the system design and laboratory testing (which are not documented elsewhere) while compiling a summary of the instrument configurations deployed to date. Next, we present first-order altimetry comparisons derived from this instrument versus coincident near-infrared (NIR) lidar measurements, thereby expanding [31], [32] in a significant manner. Lastly, and to highlight the versatility of our radar asset, we introduce data from dual-band surface measurements on firn, and initial results from airborne measurements over terrestrial snow. This article is organized as follows. Section II offers an overview of the instrument and its various subsystems. Section III provides a summary of laboratory tests and system performance. Section IV describes the different platforms and configurations used for field-testing, and presents results from four separate measurement campaigns. Finally, Section V concludes this article.

II. System Design Overview

The instrument is a multi-UWB homodyne frequency modulated continuous wave (FMCW) radar, capable of transmitting ∼ 100 mW on each band. Table I offers a summary of relevant parameters.[1] Fig. 1(a) shows a simplified block diagram of the system, which is composed of a main chassis and a *Ku*-/*Ka*-band module installed in close proximity with the antennas. Details of the subblock diagram in Fig. 1(b) are discussed in Section II-A. The main chassis [see Fig. 1(c)] contains the digital section, the chirp generator block, and the S/C RF front-end. The *Ku*-/*Ka*-band module [see Fig. 1(d)] contains the RF front-end for the other two frequency bands.

TABLE I
Summary of System Parameters

Parameter	Value	Units
Operating frequency range	2–8; 12–18; 32–38	GHz
Instantaneous bandwidth (per band)	6	GHz
Vertical resolution (snow, with Hanning smoothing window)	∼3	cm
Transmit power (per band)	∼20	dBm
Pulse duration	250	μs
Pulse repetition frequency	2–3.125	kHz
IF sampling rate	125	MSPS
ADC resolution (effective)	14 (12)	bits
Antenna type (element)	Rectangular horn	
Antenna gain	∼10–20; 20; 20	dBi
Main radar chassis weight	15	kg
Ku/Ka band module weight	10	kg
Power consumption (total)	<250	Watt

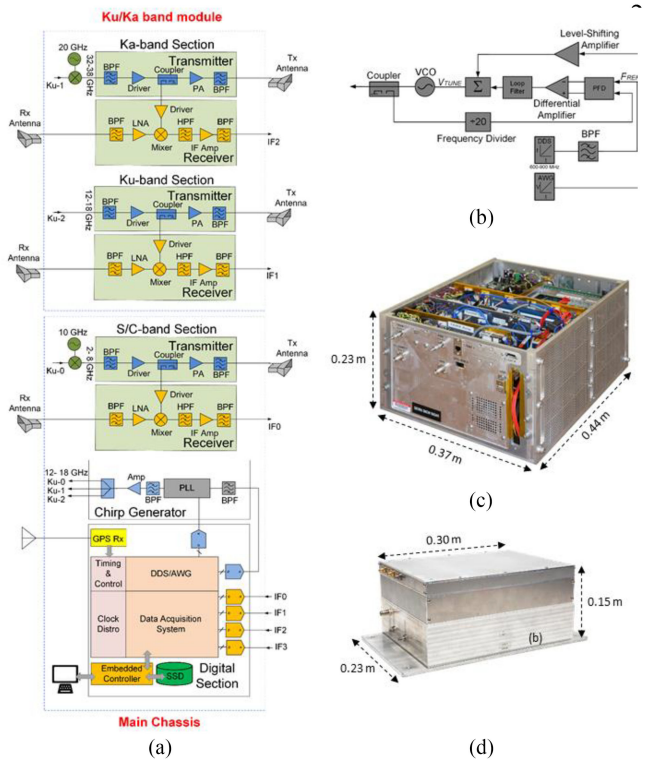

Fig. 1. (a) Simplified system block diagram. (b) Block diagram of the PLL-based chirp generator subsystem. (c) Photograph of the main radar chassis. (d) Photograph of the *Ku*-/*Ka*-module.

[1]With ∼6 GHz of bandwidth, the system provides a theoretical vertical resolution of ∼3 cm in snow, assuming a windowing factor of 1.44 and a dielectric constant of 1.53, which corresponds to a density of 0.3 g/cm^3. This resolution is likely sufficient for the assessment of firn layers on ice sheets and thick snow cover on sea ice. However, wider bandwidths are required for measuring thin snow on sea ice, as recently shown in [19]. The ability to measure snow coating thicknesses of 3 cm or less is important because thin snow influences sea ice growth. Moreover, its knowledge is important to mitigate biases in ice thickness estimates from freeboard measurements, and helps understanding natural processes in environments where flooding of the ice-snow interface is observed [34]. In principle, the bandwidth of this system can be extended via frequency multiplication, as shown in [35] and [36], or by using newer high-speed data converters combined with frequency translation stages, as done in [37].

A. Chirp Generator

The chirp generator subsystem is an improved realization of the design described in [6] and [38]. A simplified diagram of this subblock is shown in Fig. 1(b). It uses a phase-locked loop (PLL) with wide loop bandwidth and dual compensation to produce a fast, ultralinear frequency down-sweep in the $f = 12$–18 GHz range. The sweep time is 250 μs with a programmable pulse repetition frequency (PRF). The PRF is typically 2 kHz, although it can be set as high as 3.125 kHz.

The first PLL compensation is achieved by using an arbitrary waveform generator (AWG) in the digital section, which is used in combination with a level-shifting amplifier to produce a coarse-corrected tuning signal for a wideband voltage-controlled oscillator (VCO). The second compensation is obtained by phase-locking a frequency-divided replica of the 12–18 GHz VCO output ($f/20 = 600$–900 MHz) onto a down-chirp in the same band, which is produced by a direct digital synthesizer (DDS). We selected the frequency scaling factor of 20 based on the DDS clocking scheme and the phase detector chip employed (HMC440). The filtered error signal at the output of the phase detector is combined with the VCO voltage correction signal by using an op-amp-based adder. The resulting signal is a coherent microwave chirp with an rms frequency nonlinearity on the order of 10^{-4}%.

The 12–18 GHz chirp signal at the output of the VCO is power split in three ways. One of the signals is routed to the *Ku*-band transmitter, whereas the other two are down-/up-converted to the 2–8 and 32–38 GHz bands by means of two mixers driven by separate phase-locked local oscillators (PLOs) with frequencies of 10 and 20 GHz, respectively.

B. Digital Section

The AWG mentioned in Section II-A is a PXI 5422, which operates at 125 MSa/s with a 16-b resolution. The DDS is based on the AD9910 chip from Analog Devices and is operated at 1 GSa/s [39]. In addition, the digital section includes a PXIe 1071 compact chassis from National Instruments equipped with a FlexRIO field-programmable gate array (FPGA) module (7965R); a four-channel digitizer with 14-bit resolution (NI5761); a PXIe-8135 embedded computer for instrument control; and a set of redundant solid-state drives. The data acquisition system can record up to four simultaneous channels using separate analog-to-digital (ADC) converters. The ADC sampling and DDS reference signals are both 125 MHz. The reference signal for the up-/down-converting PLOs is 100 MHz. We implemented onboard averaging using the FPGA module to maintain the data rate under 20 MB/s for a single channel or under 50 MB/s for four channels. Real-time ADC multiplexing is available when a single-channel configuration is required. The instrument has a graphical user interface for changing radar settings and for real-time in-flight data display.

C. RF Front-Ends

We have three separate analog RF front ends, each one covering one of the three operating bands. The front-ends consist of a transmitter and a receiver. The transmitter filters and amplifies the signal from the chirp generator (after down-/up-conversion outside *Ku*-band) before feeding the transmit antennas (denoted as Tx in the block diagram). The receive antennas (denoted as Rx) collect multiband radar signal returns from the observed scene. The returns are bandpass filtered, amplified, and mixed with a copy of the transmit signal of each band. The mixer outputs (beat signals) are high-pass filtered, further amplified, bandpass filtered, and digitized. The total gain of the analog receivers is $\sim$50 dB. The digitizer records the beat signal from each band on separate channels. The 62.5-MHz wide Nyquist sampling bands correspond to 390 m ($\sim$1280 ft.) range windows when the full 6 GHz bandwidth is exercised. As in any FMCW system, the beat signals have a frequency spectrum that contains the range profile for each band.

D. Antennas

We use COTS rectangular horns for transmission and reception at each band, with platform-specific mounting considerations to maximize Tx/Rx isolation. For the S/C bands, we have used two configurations. The first configuration consists of a Q-Par Angus WBH2-18 for transmit (gain $\sim$10 dBi) and a Steatite Q-Par QWH-SL-2-18-SHG-R for receive (gain $\sim$20 dBi). The second configuration for S/C band consists of a set of two A-info LB-20180-NF antennas for transmit and receive (gain $\sim$10 dBi). For the *Ku*-band, we used a set of PE9854/SF-20 horns from Pasternack Enterprises, which have $\sim$20 dBi of gain and a beamwidth of 16°–23° across the band. For the *Ka*-band, we used a set of Flann 22240 antennas, whose gain is also $\sim$20 dBi. All the above antennas are linearly polarized.

III. Laboratory Tests

We conducted a series of tests to assess the performance of the radar in a laboratory setting. First, we recorded the PLL compensation signal at the output of the loop filter (before the summing amplifier), as shown in Fig. 2(a). This measurement helped verify that the loop circuit remains phase-locked to the 600–900 MHz reference across the sweep, whereas the corrected VCO tuning curve compensates for the oscillator's voltage-frequency nonlinearities. The compensation signal is nearly constant with a maximum deviation of $\pm$50 mV, indicating lock for the majority of the sweep period. We observed that during the initial 14 μs, the voltage required by this particular VCO chip exceeds the output swing of the summing amplifier. This corresponds to a $\sim$336-MHz narrow band in the upper part of the *Ku*-band sweep (5.6%), resulting in an actual frequency range at the output of the chirp generator of 12–17.67 GHz [Fig. 2(b)] and *Ku*-band transmitter [Fig. 2(d)]. Consequently, the frequency ranges at the S/C and *Ka* bands are 2–7.67 GHz [Fig. 2(e)] and 32–37.67 GHz [Fig. 2(f)], respectively. This results in a commensurate reduction in the radar's vertical resolution (3.8 cm in free space or 3.07 cm in snow) compared to the value obtained if the full 6 GHz bandwidth was available (3.6 cm in free space or 2.91 cm in snow). This reduction is small enough not to be a significant

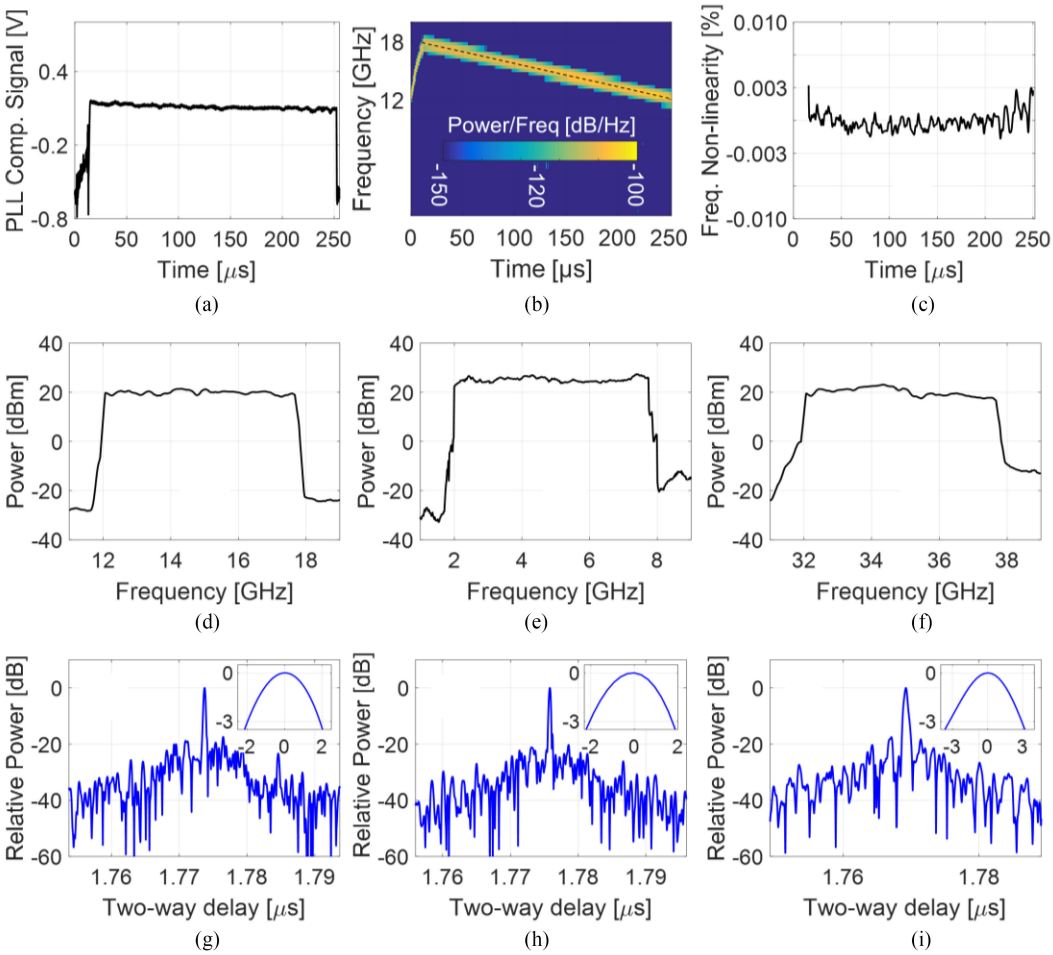

Fig. 2. Experimental results from the system's laboratory characterization: (a) PLL compensation signal; (b) spectrogram of the chirp generator's output signal; (c) measured chirp frequency nonlinearity profile; measured output spectrum of the (d) *Ku*-band transmitter, (e) S/C band transmitter, and (f) *Ka*-band transmitter. Radar system responses measured with a synthetic target for (g) *Ku*-band, (h) S/C band, and (i) *Ka*-band. The insets are zoomed views of the main peak for each response, showing relative power (in dB) versus normalized range (in cm).

issue for this work. Moreover, this limitation can be overcome by using currently available operational amplifiers with larger biasing voltages [40].

Next, we evaluated the spectral purity and frequency fidelity of the chirp generator output across the duration of the sweep. This was done using data captured with a 50-GS/s digital scope. Fig. 2(b) shows the instantaneous spectral content of the *Ku*-band chirp, which is devoid of in-band spurious signals to a level of at least –50 dBc. Fig. 2(c) shows the frequency nonlinearity profile of the chirp. The experimental rms nonlinearity is 7.8×10^{-4}%, which is adequate to maintain low near-range range sidelobes up to an altitude of 810 m (2657 ft.) AGL while exercising the full 6 GHz [19], [41].

Lastly, we performed loop-back tests for each band by using an electro-optical transceiver, a fiber optic line, cables, and attenuators to simulate a single target at ∼265 m (∼870 ft.). The total loop attenuation and time delay in the test configuration, measured separately with a vector network analyzer (VNA), were ∼110 dB and 1.769 μs, respectively. Fig. 2(g)–(i) shows the normalized response for each band obtained by applying the fast Fourier transform onto a single radar record after using a Hanning smoothing window. The target signals appear ∼40–45 dB above the noise floor, from which we infer a loop sensitivity of ∼150–155 dB. The two-way delays match the VNA measurements and reveal internal system delays of a few nanoseconds. The near-range sidelobes in the measured responses are lower than –20 dB down from the main peak, as expected from the frequency linearity shown in Fig. 2(c) and per the criteria given in [41]. The insets in Fig. 2 show a zoomed view of the main lobes after range normalization, showing a half-power width of 3.8 cm for the Ku and S/C band responses, in agreement with the range resolution expected in air for 5.67 GHz bandwidth and a windowing factor of 1.44. For the *Ka*-band response, the half-power width is broader (∼6 cm). This degradation stems partly from the frequency roll-off inherent to the *Ka*-band RF front-end, but mostly from the response of the electro-optical modulator used in the setup. Its insertion gain presents a 12 dB variation in the 35–38 GHz range. This reduces the effective bandwidth of the measurement, thus degrading the radar's range resolution. The free-space vertical resolution inferred from airborne measurements over a smooth surface after deconvolution, as is shown in Section IV-C, is ∼4 cm (3.2 cm in

Fig. 3. Photographs showing the instrument and antenna configurations for different test platforms. (a) Integration on the NASA SIERRA UAS (not flown). (b) Integration on a de Havilland DCH-3 Single Otter for S/C band field trials in Alaska. (c) Integration on a de Havilland DHC-6 Twin Otter for *Ku*-/*Ka*-band field trials in Greenland and Arctic sea ice. (d) Surface-based test setup for firn measurements on the Greenland Ice Sheet. (e) Instrument configuration on a Cessna 172 for S/C band trials to measure terrestrial snow cover in South Dakota.

snow), which is closer to the 3.8 cm (3.07 cm in snow) predicted from theory.

IV. Field Trials

A. Test Platforms

We originally designed the instrument to operate at the S/C bands onboard the NASA SIERRA UAS in 2013. In July 2013, we integrated it onto one of the payload noses and ground tested it, but we did not have an opportunity to fly it because the UAS was lost prior to the first radar mission [42]. Fig. 3(a) shows photographs of the system integrated onto payload nose B, which included the radar transmit antenna, the main radar chassis, and a Riegl Q-240i scanning lidar. The receive antenna was mounted in the airframe (not shown).

In May 2018, we operated the radar for the first time during a science mission onboard a de Havilland DHC-3 Single Otter. We used it to measure snow cover thickness in various regions of Alaska using S/C bands. The transmit antenna was installed in the nose of the aircraft. To do this, we replaced an existing inspection panel and used it as a nadir port covered with a dielectric radome. The Rx antenna was installed through an opening in the aft area of the aircraft, next to a Riegl LMS Q-240i-type lidar provided by the University of Alaska, Fairbanks, which operates at an NIR wavelength of 905 nm [31]. During the transit flights to the survey site in this mission, we also collected data of opportunity in vegetated areas and measured tree canopy height [33]. In May 2021, we conducted a follow-up field campaign with the same general configuration.

In August 2019, we operated the radar system on a DHC-6 Twin Otter airplane to test its dual-band altimetry capabilities at *Ku*- and *Ka*-bands [32]. Fig. 3(c) shows photographs of that installation, with the main radar chassis located in the cabin and the *Ku*-/*Ka*-band RF front end and antennas in the aft luggage compartment/nadir port. The instrument payload included inertial navigation units, global positioning system receivers, and a Riegl LMS Q-240i-60 lidar operating at an NIR wavelength of 904 nm, which was provided by the National Space Institute, Technical University of Denmark (DTU Space).

In April 2019, we tested the system on the Greenland Ice Sheet using a quick-deployable surface-based configuration intended to take measurements at *Ku*- and *Ka*-bands on the top part of the firn column [see Fig. 3(d)]. We installed the antennas on a beam, which we extended through the back door of a carrier DHC-6 at each measurement site. We performed several single-point measurements and one kinematic test in which we collected data while taxiing the aircraft before take-off.

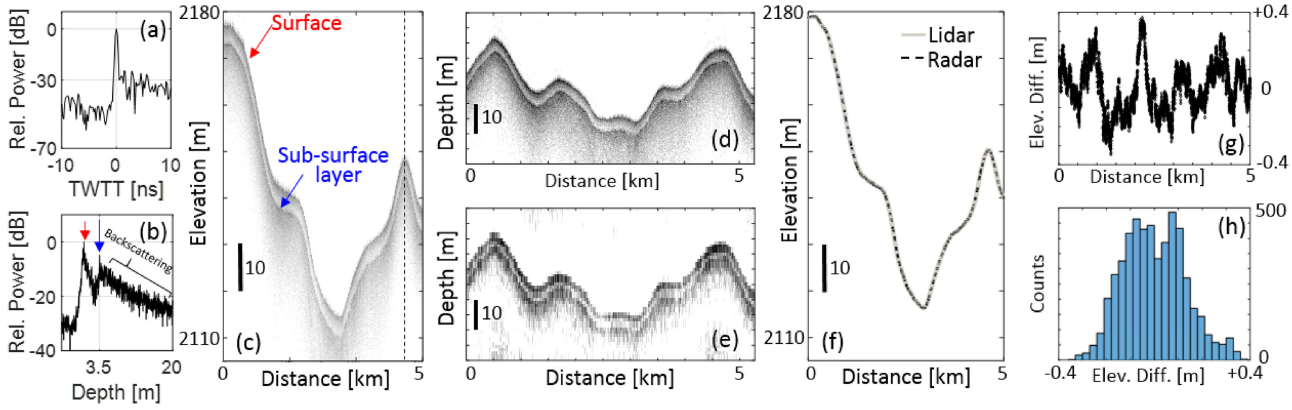

Fig. 4. Results from the S/C band measurements in Alaska onboard the Single Otter: (a) In-flight radar response measured over a smooth surface; (b) relative received power versus two-way travel time recorded at the location marked with -- in the echogram; (c) radar image demonstrating the system's ability to map snow cover thickness. The same frame processed without elevation corrections using the (d) full bandwidth; and with (e) 100 MHz bandwidth; (f) radar- and lidar-derived surface elevations for the same data frame; (g) difference between radar- and lidar-inferred surface elevations; and elevation offset histogram.

In February 2020, we operated the system onboard a Cessna 172 [see Fig. 3(e)] to evaluate the suitability of the system to measure terrestrial snow cover. We placed the main radar chassis in the aft luggage compartment, whereas the antennas were installed on the wing struts.

B. S/C Band Airborne Tests in Alaska

With the configuration shown in Fig. 3(b), we successfully mapped seasonal snow cover layers in Alaska, with thicknesses ranging from 30 cm to 15 m at low elevations above mean sea level (AMSL) and at to least 85 m in high AMSL elevation regions, where the snow is colder [31]. Fig. 4(a) shows the response obtained over a relatively smooth surface (low backscattering intensity) from an altitude of 348 m AGL. Fig. 4(b) shows the normalized power profile for the range line marked by the dotted line in the echogram of Fig. 4(c). The surface and subsurface radar returns are marked with a red and blue arrow, respectively. Fig. 4(c) shows a sample radar image from the data captured at an average altitude of 300 m above the surface of Walsh glacier (Frame ID 20180523_04_008). The data were processed with the CReSIS toolbox [43]. We assumed a dielectric constant of 1.53 to infer a snow layer thickness of ∼3.5 m at that particular location.

To show the utility of this system to simulate different operating parameters through the spectral segmentation of UWB data, Fig. 4(d) and (e) shows the same 20180523_04_008 frame processed with 6 GHz and 100 MHz bandwidth, respectively. Unlike Fig. 4(c), we did not apply elevation corrections to these echograms, as we only wanted to highlight differences in the quality of the images produced with two distinct bandwidth settings. When using 100 MHz bandwidth, the radar furnishes a vertical resolution of 1.7 m in snow, which is still sufficient to resolve the subsurface interface at a depth of 3.5 m. Although there is a clear degradation in the dynamic range and overall quality of the subbanded image, such processing allows us to evaluate differences in backscattering signatures and the suitability of various frequency bands for different measurement scenarios.

Fig. 4(f) compares the snow surface elevation mapped through simultaneous radar and lidar measurements. We found that the two measured vertical profiles were offset by 13.2 ns, resulting from system delay differences between the two instruments. After compensating for this constant offset, the two surface altitudinal records were in good agreement to the first degree. Fig. 4(g) shows a plot of the differences between the radar- and lidar-derived elevation profiles along the 5-km flight segment (5275 points) after correcting for the aforementioned constant offset. Fig. 4(h) shows the corresponding frequency distribution histogram. The difference in elevations has a mean value of zero with a standard deviation of 0.128 m.

C. Ku/Ka-*Band Airborne Tests in Greenland*

For this mission, we used the configuration shown in Fig. 3(c) as a trial run in support of CryoSat-2 and ICESat-2 data validation. We conducted test flights in Iceland, a transit flight over the East Greenland Ice Sheet margin, and two flights over Arctic sea ice out of Station Nord. Fig. 5(a) and (b) shows the specular responses (after deconvolving system effects) measured over an open lead (seawater) in the Arctic Ocean. Sea ice leads do not have snow coating and behave as mirror-like surfaces for radar signals at these frequencies (ideally with no volume scattering). We used these measurements to calibrate the system and verify its sensitivity. The signal-to-noise ratios (SNRs) obtained in these plots are ∼40 dB at *Ka*-band to ∼60 dB at *Ku*-band. This shows that the system has sufficient sensitivity to conduct dual-band altimetry measurements. The disparities in received power levels are consistent to the higher propagation losses at *Ka*-band and slight differences in transmit power.

Fig. 5(c)–(e) shows sample echograms from coincident dual-band height retrievals over the Greenland Ice Sheet margin (frame ID 20190810_02_001). The *Ku*-band signal offered some penetration and the ability to resolve a subsurface layer at an

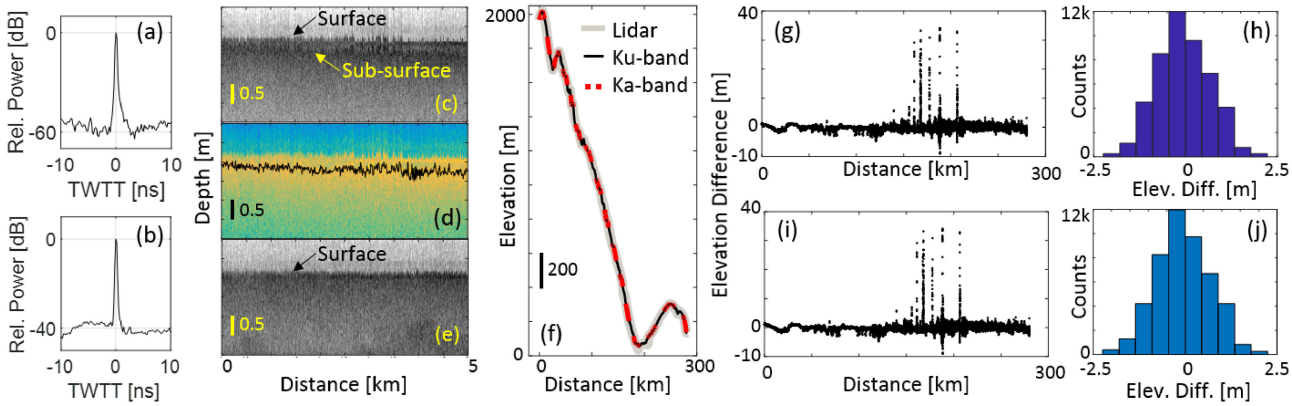

Fig. 5. Results from the coincident *Ku*-/*Ka*-band and lidar measurements in Greenland onboard the Twin Otter: Normalized received waveforms from tests over a sea ice lead (after deconvolution) from (a) *Ku*-band and (b) *Ka*-band; elevation-corrected echogram from height retrievals over the Greenland Ice Sheet periphery using (c) *Ku*-band; (d) same data frame with the subsurface interface tracked; (e) elevation-corrected echogram from *Ka*-band data. (f) Comparison between lidar and dual-band radar altimetry data across 56 contiguous frames over the Greenland Ice Sheet margin; (g) elevation differences between lidar and *Ku*-band radar data after systematic offset corrections and (h) corresponding distribution histogram; (i) elevation difference between lidar and *Ka*-band radar data and (j) corresponding distribution histogram.

average depth of 30 cm assuming the same dielectric constant of 1.53. This interface is tracked in Fig. 5(d) and not visible in the *Ka*-band echogram of Fig. 5(e).

We used data from the onboard laser scanner to perform initial comparisons of the radar-inferred height retrievals. Fig. 5(f) shows the surface topography variations derived from dual-band radar and lidar data for 56 consecutive frames, which corresponds to 280 linear km. We obtained a first-order match between the radar and lidar-derived elevations after correcting for intrinsic delay offsets of less than 13 ns.

Fig. 5(g) shows the elevation differences between the lidar and the *Ku*-band radar altimetry profiles over 48 584 points. Large elevation differences of up to 34 m occurred in areas with complex topography (e.g., regions with crevasses or with precipitous slopes). The corresponding frequency distribution histogram with outliers removed (98.7% of the points being counted) is shown in Fig. 5(h). We obtained nearly identical results when comparing the lidar minus *Ka*-band radar offsets along the survey line, as shown in Fig. 5(i) and (j). The mean value of the elevation differences for both comparisons is close to zero, with a standard deviation of 0.71 m.

These results indicate that the surface elevation readings obtained with the *Ku*- and *Ka*-band radar signals are highly consistent with one another. Fine-scale offsets in surface height retrievals obtained from lidar and radar data are expected based on previous studies [44], [45]. These differences are not straightforward to interpret, though, because they stem from a variety of factors, including the unequal surface illuminations between the multi-UWB radar and the lidar, terrain-induced errors, snow surface conditions and interactions, and the choice of the surface-tracking algorithm. Although further analyses will be required to better understand these differences, our initial results show the feasibility of using our instrument to carry out dual-band radar altimetry measurements.

Fig. 6 shows some results to illustrate how coincidental UWB radar data can be spectrally segmented to simulate the operation

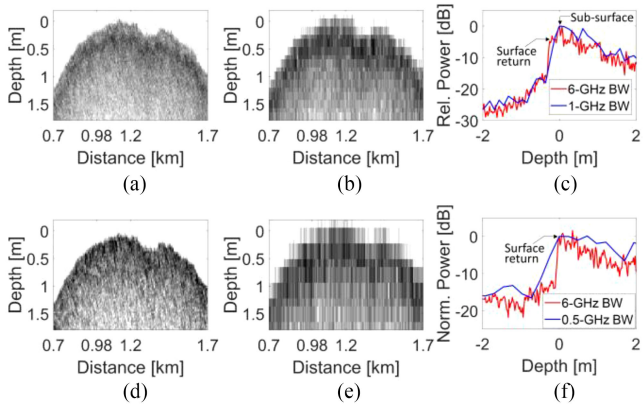

Fig. 6. Results illustrating full-bandwidth and subbanded processing to emulate the operating parameters of the ASIRAS and AltiKA instruments, respectively: (a) *Ku*-band data frame without altitude corrections processed with 6 GHz bandwidth; (b) same frame processed with 1 GHz bandwidth at a center frequency of 13.5 GHz; (c) A-scopes comparing the *Ku*-band received power profiles with full and reduced bandwidth for one range line. (d) *Ka*-band data frame without altitude corrections processed with 6 GHz bandwidth; (e) same frame processed with 0.5 GHz bandwidth at a center frequency of 35.75 GHz; (f) A-scopes comparing the *Ka*-band received power profiles with full and reduced bandwidth for one range line.

of other instruments. Fig. 6(a) shows a portion of the same *Ku*-band frame ID 20190810_02_001 between 0.7 and 1.7 km from the beginning of the segment, without elevation corrections and processed with the full 6 GHz bandwidth. Fig. 6(b) shows the same frame processed with a center frequency of 13.5 GHz and 1 GHz bandwidth to emulate the operation of the ASIRAS instrument in its widest bandwidth configuration [22]. Fig. 6(c) shows the normalized received power profiles as a function of depth for the range line #190 (km marker 0.98). The range profiles were shifted horizontally so that zero aligns with the power maxima. From this plot, we observed that the subsurface interface is brighter than the surface. The subbanded data may thus lead to ambiguity in the determination of the

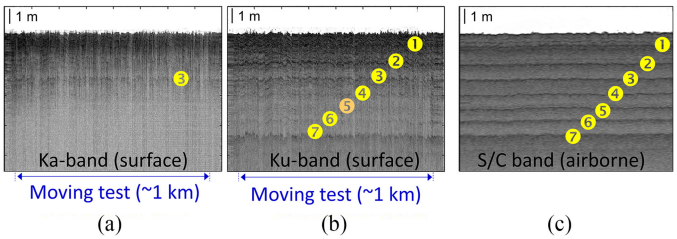

Fig. 7. Radar images from multifrequency data collection in the interior of the Greenland Ice Sheet: (a) *Ka*-band surface data; (b) *Ku*-band surface data; and (c) S/C band airborne data. The numbers indicate the various internal reflecting horizons (IRHs) mapped with the instruments.

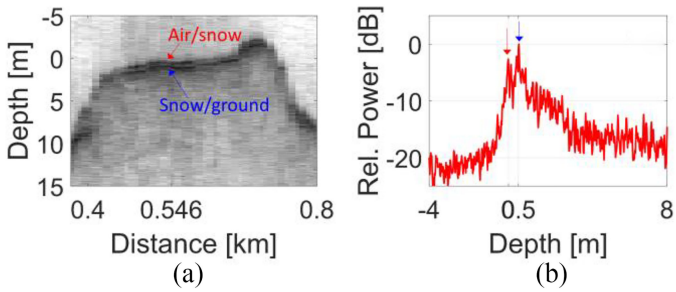

Fig. 8. Initial results from data collected over snow-covered ground onboard the Cessna 172 using 2.5–8 GHz: (a) radar echogram; and (b) relative received power profile for km marker 0.546 in the echogram.

surface location, whereas the full-bandwidth data resolve both interfaces distinctly.

Fig 6(d) shows the same frame for the *Ka*-band data processed with full bandwidth. Fig. 6(e) shows the corresponding frame subbanded to match the operating parameters of the SARAL AltiKa instrument (35.75 GHz center frequency with 500 MHz of bandwidth) [46]. Fig. 6(f) shows the corresponding normalized A-scopes aligned to the surface location. The differences in signal penetration and the dominance of the power coming from the surface and subsurface for *Ka*- and *Ku*-band signals can be used to infer the thickness of snow layers, even with narrow band data [11], [47], whereas the UWB data are a valuable verification tool for the unambiguous identification of shallow subsurface interfaces.

D. Ku/Ka-*Band Surface Tests in Greenland*

By taking advantage of the instrument portability and reconfigurability, we used it for localized studies of the ice sheet firn column. Fig. 7 shows preliminary results from a surface-based dual-band *Ku*-/*Ka*-band acquisition in the interior of the Greenland Ice Sheet. We used the configuration shown in Fig. 3(d) during a moving test while taxiing, as mentioned in Section IV-A. The extent of the survey was ∼1 km. For reference, the data are compared against a nearly coincident line from NASA OIB using our other UWB (2–18 GHz) snow radar sounder (Frame ID 20190512_01_647) [19]. The mapped IRHs are marked with numbers 1–7, where #7 (located at a depth of ∼5 m) corresponds to the 2012 melt event [48]. The airborne radar system is able to map these IRHs with the sharpest detail [see Fig. 7(c)], because of the lower frequencies of operation and consequently higher signal penetration. As expected, the *Ka*-band signal has much less penetration, and our system only maps the IRH at 3 m below the surface very faintly with that band [Fig. 7(a)], whereas the *Ku*-band signal [Fig. 7(b)] maps the same interfaces that are sounded with the airborne system. The IRH #5 in Fig. 7(b) is mostly discernible when the radar was static.

E. *S/C Band Airborne Tests in South Dakota*

We collected data in the Black Hills of South Dakota onboard the Cessna 172 with the configuration shown in Fig. 3(e). The purpose of these tests was to evaluate the suitability of S/C band frequencies for retrieval of snow cover over land. We operated the radar in the 2.5–8 GHz range to comply with local spectral management restrictions. Fig. 8(a) shows an echogram produced with data collected with the system in an area where the snow cover is ∼0.5 m thick (frame ID Data_20200129_01_024). The A-scope corresponding to range line #60 (km marker 0.546) is shown in Fig. 8(b). The air/snow interface is detected with ∼17 dB SNR, whereas the snow/ground interface is ∼3 dB stronger.

This data set is still being analyzed, along with results from a more recent multichannel configuration used in 2021 to overcome limitations in areas with sophisticated topography and rough snow surface conditions.

V. Conclusion

We developed a compact, airborne multi-UWB radar for snow-layer thickness evaluation and altimetry measurements. The instrument operates in FMCW mode over three separate bands with up to ∼18 GHz cumulative bandwidth and sweep frequency nonlinearities of $\sim 10^{-4}$%. We demonstrated its operation effectiveness under different scenarios using both surface and airborne configurations over a variety of targets. We verified our multiband radar altimetry data through coincidental lidar measurements, showing good first-degree agreement between datasets after ns-scale offset corrections. We also encountered fine-scale height retrieval differences consistent with previous studies performed with coarser-resolution radar. We demonstrated the utility of full-bandwidth data to yield cm-scale vertical resolution or subbanded data to emulate the operating parameters of satellite instruments. We showed that this system has potential application to firn composition studies and retrieval of terrestrial snow cover thickness.

Acknowledgment

The authors would like to thank Dr. J. Holt and Dr. M. Truffer for their support during the Alaska experiment. The authors gratefully acknowledge Dr. A. Hogg, Dr. S. Simonsen, Dr. L. Sandberg Sorensen, and I. Otosaka for the support they provided during the ground and airborne campaigns in Greenland. The authors would also like to thank Dr. J. Paden and B. Miller for processing one of the data frames. The authors recognize A. Paden, K. T. Karidi, and P. Place for their support with equipment preparations.

REFERENCES

[1] N. Galin, A. Worby, T. Markus, C. Leuschen, and P. Gogineni, "Validation of airborne FMCW radar measurements of snow thickness over sea ice in Antarctica," *IEEE Trans. Geosci. Remote Sens.*, vol. 50, no. 1, pp. 3–12, Jan. 2012.

[2] R. Jenssen, M. Eckerstorfer, and S. Jacobsen, "Drone-mounted ultrawideband radar for retrieval of snowpack properties," *IEEE Trans. Instrum. Meas.*, vol. 69, no. 1, pp. 221–230, Jan. 2020.

[3] R. L. Hawley, E. Morris, R. Cullen, U. Nixdorf, A. Shepherd, and D. Wingham, "ASIRAS airborne radar resolves internal annual layers in the dry-snow zone of Greenland," *Geophys. Res. Lett.*, vol. 33, 2006, Art. no. L04502.

[4] R. Willatt, S. Laxon, K. Giles, R. Cullen, C. Haas, and V. Helm, "Ku-band radar penetration into snow cover on Arctic sea ice using airborne data," *Ann. Glaciol.*, vol. 52, no. 57, pp. 197–205, 2011, doi: 10.3189/172756411795931589.

[5] J. B. Yan *et al.*, "Airborne measurements of snow thickness: Using ultra-wideband frequency-modulated-continuous-wave radars," *IEEE Geosci. Remote Sens. Mag.*, vol. 5, no. 2, pp. 57–76, Jun. 2017.

[6] D. Gomez-Garcia, F. Rodriguez-Morales, C. Leuschen, and S. Gogineni, "Ku-Band radar altimeter for surface elevation measurements in polar regions using a wideband chirp generator with improved linearity," in *Proc. IEEE Geosci. Remote Sens. Int. Symp.*, Munich, Germany, Jul. 2012, pp. 4617–4620.

[7] S. Farrell *et al.*, "A first assessment of icebridge snow and ice thickness data over Arctic sea ice," *IEEE Trans. Geosci. Remote Sens.*, vol. 50, no. 6, pp. 2098–2111, Jun. 2012.

[8] I. Lawrence, M. Tsamados, J. Stroeve, T. Armitage, and A. Ridout, "Estimating snow depth over Arctic sea ice from calibrated dual-band radar freeboards," *Cryosphere*, vol. 12, pp. 3551–3564, 2018.

[9] G. Quartly *et al.*, Retrieving sea level and freeboard in the Arctic: A review of current radar altimetry methodologies and future perspectives," *Remote Sens.*, vol. 11, 2019, Art. no. 881.

[10] M. Kern *et al.*, "The Copernicus Polar Ice and Snow Topography Altimeter (CRISTAL): Expected mission contributions," *Cryosphere*, vol. 14, 2020, pp. 2235–2251. [Online]. Available: https://doi.org/10.5194/tc-2020-3

[11] K. Guerreiro, S. Fleury, E. Zakharova, F. Rémy, and A. Kouraev, "Potential for estimation of snow depth on Arctic sea ice from Cryosat-2 and SARAL/AltiKa missions," *Remote Sens. Environ.*, vol. 186, pp. 339–349, 2016.

[12] S. Simonsen, S. Sorensen, L. Stenseng, and R. Forsberg, "Dual frequency radar altimetry-measuring Greenland firn properties from space," in *Proc. 25 Years Prog. Radar Altimetry Symp.*, Ponta Delgada, Portugal, 2018.

[13] G. Koh, N. Yankielun, and A. I. Baptista, "Snow cover characterization using multiband FMCW radars," *Hydrol. Processes*, vol. 10, pp. 1609–1617, 1996.

[14] J. Scott, D. Mair, P. Nienow, V. Parry, and E. Morris, "A ground-based radar backscatter investigation in the percolation zone of the Greenland ice sheet," *Remote Sens. Environ.*, vol. 104, pp. 361–373, 2006.

[15] H. P. Marshall and G. Koh, "FMCW radars for snow research," *Cold Regions Sci. Technol.*, vol. 52, pp. 118–131, 2008.

[16] R. Willatt, K. Giles, S. Laxon, L. Stone-Drake, and A. Worby, "Field investigations of Ku-band radar penetration into snow cover on Antarctic sea ice," *IEEE Trans. Geosci. Remote Sens.*, vol. 48, no. 1, pp. 365–372, Jan. 2010.

[17] J. Stroeve, "Surface based Ku- and Ka-band polarimetric radar for sea ice studies," *Cryosphere*, vol. 14, pp. 4405–4426, 2020.

[18] B. Panzer *et al.*, "An ultra-wideband, microwave radar for measuring snow thickness on sea ice and mapping near-surface internal layers in polar firn," *J. Glaciol.*, vol. 59, no. 214, pp. 244–254, 2013, doi: 10.3189/2013JoG12J128.

[19] F. Rodriguez-Morales *et al.*, "An improved UWB microwave radar for very long-range measurements of snow cover," *IEEE Trans. Instrum. Meas.*, vol. 69, no. 10, pp. 7761–7772, Oct. 2020.

[20] J. Li *et al.*, "Airborne measurements of a Ka-band radar altimeter over Greenland land ice and Arctic sea ice," in *Proc. Int. Glaciol. Soc. Symp.*, Stanford, CA, USA, Jul. 2019.

[21] C. J. Leuschen and R. K. Raney, "Initial results of data collected by the APL D2P radar altimeter over land and sea ice," *Johns Hopkins APL Tech. Dig.*, vol. 26, no. 2, pp. 114–122, 2005.

[22] Accessed Jun. 2021. [Online]. Available: https://earth.esa.int/web/eoportal/airborne-sensors/asiras

[23] 2019, Accessed Jun. 2021. [Online]. Available: https://earth.esa.int/eogateway/documents/20142/1526226/CryoVEx2017-final-report.pdf

[24] A. Tan, K. Eccleston, I. Platt, I. Woodhead, W. Rack, and J. McCulloch, "The design of a UAV mounted snow depth radar: Results of measurements on Antarctic sea ice," in *Proc. IEEE Conf. Antenna Meas. Appl.*, Tsukuba, Japan, Feb. 2017, pp. 316–319.

[25] M. Oyan, S. Hamran, L. Damsgard, and T. Berger, "Compact airborne C-Band radar sounder," *IEEE Trans. Geosci. Remote Sens.*, vol. 52, no. 10, pp. 6323–6332, Oct. 2014.

[26] Y. Kim *et al.*, "A Ku-band CMOS FMCW radar transceiver for snowpack remote sensing," *IEEE Trans. Microw. Theory Techn.*, vol. 66, no. 5, pp. 2480–2494, May 2018.

[27] P. Pomerleau *et al.*, "Low cost and compact FMCW 24 GHz radar applications for snowpack and ice thickness measurements," *Sensors*, vol. 20, no. 14, Jul. 2020, Art. no. 3909, doi: 10.3390/s20143909.

[28] R. Rincon, B. Osmanoglu, P. Racette, Q. Bonds, and M. Perrine, "Tri-frequency synthetic aperture radar for the measurements of snow water equivalent," in *Proc. IEEE Int. Geosci. Remote Sens. Symp.*, Yokohama, Japan, Jul./Aug. 2019, pp. 8653–8655.

[29] K. Speed *et al.*, Air Campaign Results for the Wideband Instrument for Snow Measurements (WISM). Jun. 2015. [Online]. Available: https://esto.nasa.gov/forums/estf2015/presentations/Durham_S5P3_ESTF2015.pdf

[30] J. MacGregor *et al.*, "The scientific legacy of NASA's Operation Icebridge," *Rev. Geophys.*, vol. 59, no. 2, Jun. 2021, Art. no. e2020RG000712.

[31] J. Li *et al.*, "Airborne snow measurements over Alaska mountains and glaciers with a compact FMCW radar," in *Proc. IEEE Int. Geosci. Remote Sens. Symp.*, Yokohama, Japan, Jul./Aug. 2019, pp. 3966–3969.

[32] F. Rodriguez-Morales, J. Li, C. Leuschen, S. Hvidegaard, and R. Forsberg, "Airborne altimetry measurements in the arctic using a compact multi-band radar system: Initial results," in *Proc. IEEE Geosci. Remote Sens. Int. Symp.*, Sep./Oct. 2020, pp. 3019–3022.

[33] J. Li *et al.*, "Comparison of coincident forest canopy measurements from airborne lidar and ultra-wideband microwave radar," in *Proc. IEEE Geosci. Remote Sens. Int. Symp.* Brussels, Belgium, Jul. 2021.

[34] A. Rosel *et al.*, "Implications of surface flooding on airborne thickness measurements of snow on sea ice," *Cryosphere*, vol. 155, pp. 2819–2833, 2020. [Online]. Available: https://doi.org/10.5194/tc-2020-168

[35] J. B. Yan *et al.*, "Ultra-Wideband FMCW radar for airborne measurements of snow over sea-ice and land," *IEEE Trans. Geosci. Remote Sens.*, vol. 55, no. 2, pp. 834–843, Feb. 2017.

[36] H. Talasila, "Modular frequency multiplier and filters for the NASA global hawk snow radar," M.S. thesis, Dept. Elect. Eng. Comput. Sci., Univ. Kansas, Lawrence, KS, USA, 2017.

[37] K. Carr, "Development of a multichannel wideband radar demonstrator," M.S. thesis, Dept. Elect. Eng. Comput. Sci., Univ. Kansas, Lawrence, KS, USA, 2019.

[38] D. Gomez-Garcia, "A linearization method for a UWB VCO-based chirp generator using dual compensation," M.S. thesis, Dept. Elect. Eng. Comput. Sci., Univ. Kansas, Lawrence, KS, USA, 2011.

[39] J. Ledford, "Development of an eight channel waveform generator for beam-forming applications," M.S. thesis, Dept. Elect. Eng. Comput. Sci., Univ. Kansas, Lawrence, KS, USA, 2008.

[40] D. Gomez-Garcia, "Scattering analysis and ultra-wideband radar for high-throughput phenotyping of wheat canopies," Ph.D. dissertation, Dept. Elect. Eng., Univ. Kansas, Lawrence, KS, USA, 2019.

[41] P. V. Brennan, Y. Huang, M. Ash, and K. Chetty, "Determination of sweep linearity requirements in FMCW radar systems based on simple voltage-controlled oscillator sources," *IEEE Trans. Aerosp. Electron. Syst.*, vol. 47, no. 3, pp. 1594–1604, Jul. 2011.

[42] J. Maslanik, "Investigations of spatial and temporal variability of ocean and ice conditions and near the marginal ice zone: The marginal ice zone observations and processes experiment (MIZOPEX). Final campaign summary," DOE ARM Climate Res. Facility, Office Sci., Office Biol. Environ. Res., Washington, DC, USA, Tech. Rep. DOE/SC-ARM-15-046, Feb. 2016. [Online]. Available: https://www.osti.gov/servlets/purl/1242825

[43] CReSIS, CReSIS Toolbox, Computer Software, Lawrence, KS, USA, 2021. [Online]. Available: https://git.cresis.ku.edu/ct/

[44] C. Leuschen *et al.*, "Combination of laser and radar altimeter height measurements to estimate snow depth during the 2004 Antarctic AMSR-E sea ice field campaign," *J. Gephys. Res.*, vol. 113, 2008, Art. no. C04S90.

[45] K. Giles *et al.*, "Combined airborne laser and radar altimeter measurements over the Fram Strait in May 2002," *Remote Sens. Environ.*, vol. 111, pp. 182–194, 2007.

[46] Accessed Jun. 2021. [Online]. Available: https://directory.eoportal.org/web/eoportal/satellite-missions/s/saral

[47] R. Ricker *et al.*, "Airborne evaluation of dual-band frequency satellite radar altimetry measurements over Arctic sea ice," in *Proc. Amer. Geophys. Union, Fall Meeting*, 2018.
[48] S. Nghiem *et al.*, "The extreme melt across the Greenland ice sheet in 2012," *Geophys. Res. Lett.*, vol. 39, 2012, Art. no. L20502.

Fernando Rodríguez-Morales (Senior Member, IEEE) received the B.S. degree in electronics engineering from the Universidad Autónoma Metropolitana, Mexico City, Mexico, in 1999, and the M.S. and Ph.D. degrees in electrical and computer engineering from the University of Massachusetts, Amherst, MA, USA, in 2003 and 2007, respectively.

He is currently a Senior Scientist with the Center for Remote Sensing of Ice Sheets, University of Kansas (KU), Lawrence, KS, USA, and holds a courtesy appointment with the Department of Electrical Engineering and Computer Science, KU. He has conducted extensive fieldwork in Antarctica, Greenland, Iceland, Alaska, and Patagonia. His current technical interests include extending the capabilities of UWB radar instruments, as well as packaging, miniaturization and hardening of advanced high-frequency systems.

Dr. Rodríguez-Morales was the recipient of Graduate Fellowships from Mexico's National Institute for Astrophysics, Optics and Electronics and the National Council for Science and Technology; the U.S. Antarctic Service Medal; and three NASA Agency Honor Awards.

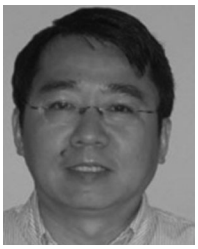

Jilu Li (Senior Member, IEEE) received the B.S. and M.S. degrees in aeronautics from Northwestern Polytechnical University, Xi'an, China, in 1985 and 1988, respectively, and the Ph.D. degree in aeronautics from Beijing University of Aeronautics and Astronautics, Beijing, China, in 1992. He received the M.S. degree in aerospace engineering, and M.S. and Ph.D. degrees in electrical engineering from the University of Kansas, Lawrence, KS, USA, in 2003, 2006, and 2009, respectively.

From 1992 to 1994, he was a Postdoctoral Research Fellow with the Beijing Aerospace Automatic Control Institute. From 1994 to 2000, he was a Senior Engineer with the Beijing Institute of Control Engineering. From 2009 to 2010, he was a Senior Engineer with LinkQuest, Inc., San Diego, CA, USA. Since 2011, he has been a research faculty member with the Center for Remote Sensing of Ice Sheets, University of Kansas. He has been participating in field experiments in Antarctica, Greenland, and Alaska, since 2011. His research interests are in developing advanced signal and array processing algorithms for processing and interpreting data of ice sheet radio-echo sounding.

Dr. Li is a member of the International Glaciology Society.

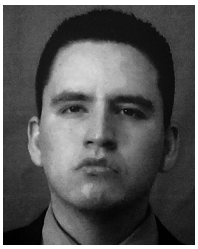

Daniel Gomez-García Alvestegui (Member, IEEE) received the B.S., M.S., and Ph.D. (hons.) degrees in electrical engineering from the University of Kansas (KU), Lawrence, KS, USA, in 2008, 2011, and 2019, respectively.

Since 2010, he has been with the Center for Remote Sensing of Ice Sheets, KU, where he is currently a Postdoctoral Researcher. His research interests include microwave remote sensing, radar systems, and electromagnetic scattering.

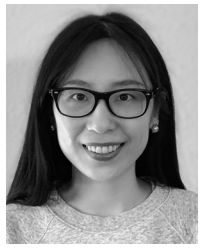

Jiaxuan (Betty) Shang received the B.S. degree in electrical engineering from The George Washington University, Washington, DC, USA, in 2013, and the M.S. degree in electrical engineering from Columbia University, New York, NY, USA, in 2015.

From 2017 to 2021, she was a Research Engineer with the Center for Remote Sensing of Ice Sheets (CReSIS), University of Kansas, Lawrence, KS, USA. At CReSIS, she contributed to the development of the digital backend of various radar systems, and supported field data collection in cold regions.

Emily J. Arnold (Member, IEEE) received the B.S. degree in aerospace engineering and Ph.D. degree in aerospace engineering from the University of Kansas (KU), Lawrence, KS, USA, in 2009 and 2013, respectively.

She is currently an Assistant Professor with the Aerospace Engineering Department, KU. She has served as the Lead Design and Structural Engineer for several airborne antenna arrays used for remote sensing ice sheets in Antarctica and Greenland. Prior to returning to KU as an Assistant Professor, she was with the MITRE Corporation.

Dr. Arnold was the recipient of two NASA Earth and Space Science Fellowships and the Zonta International's Amelia Earhart Fellowship.

Carlton J. Leuschen (Member, IEEE) received the B.S. (with highest distinction), M.S., and Ph.D. (with hons.) degrees in electrical engineering from the Radar Systems and Remote Sensing Laboratory, University of Kansas (KU), Lawrence, KS, USA, in 1995, 2001, and 2003, respectively.

He is currently a Professor with the Department of Electrical Engineering and Computer Science and the Director of the Center for Remote Sensing of Ice Sheets, KU. Prior to joining KU in 2006, he was a Senior Professional Staff Member with the Space Department, Applied Physics Laboratory, Johns Hopkins University, Laurel, MD, USA. He was a Participating Scientist in two projects involving radar sounders for Mars exploration. His research interests include the application of radar technologies for airborne measurements of ice sheets and radar sounding for planetary applications.

Dr. Leuschen was the recipient of the Richard and Wilma Moore Thesis Award and a NASA Graduate Student Research Fellowship to develop a ground-penetrating radar for Mars.

Christopher F. Larsen received the B.S. degree in physics from the University of Alaska Fairbanks, Fairbanks, AK, USA, in 1991, the M.S. degree in geophysics from the University of California, Santa Cruz, CA, USA, in 1996, and the Ph.D. degree in geophysics from the University of Alaska Fairbanks, in 2003.

He is currently a Research Professor with the Geophysical Institute, University of Alaska Fairbanks. His research interests include the study of glacier phenomena, airborne LiDAR and photogrammetry, GPS geodesy and surveying, among others.

Andrew Shepherd received the Ph.D. degree in physics from the University of Leicester, Leicester, U.K., in 1998.

He is currently a Professor of Earth Observation with the University of Leeds, Leeds, U.K., where he is also the Director of the Natural Environment Research Council Centre for Polar Observation and Modeling. He is also a Principal Scientific Advisor to the European Space Agency CryoSat Satellite Mission and the Co-Leader of the ESA-NASA Ice Sheet Mass Balance Intercomparison Exercise. His current research interests include measuring changes of the Antarctic and Greenland Ice Sheets, on understanding their interaction with the global climate system and on establishing their contribution to global sea-level rise.

Sine Munk Hvidegaard received the Ph.D. degree in geophysics from the University of Copenhagen, Copenhagen, Denmark, in 2005, with a focus on airborne ice altimetry methods for the calibration and validation of CryoSat.

She is currently a Senior Advisor with the National Space Institute (DTU Space), Technical University of Denmark, Kongens Lyngby, Denmark, where she has continued her research on remote sensing of the cryosphere and earth observations from aircraft and satellite, especially for satellite validation purposes.

René Forsberg received a double M.Sc. degree in geophysics and geodesy from The University of Copenhagen, Denmark, in 1980.

He is currently a Professor with National Space Institute (DTU Space), Technical University of Denmark, Kongens Lyngby, Denmark, and leading the European Space Agency Climate Change Initiative for Greenland. He has worked extensively with geodetic, satellite, and airborne research for cryosphere monitoring, general geodesy, and earth observation. He has taken the initiatives to, planned, and led numerous field expeditions in Greenland, Svalbard, Arctic Canada, Arctic Ocean, Antarctica, as well as many regions of Asia and Africa, both as part of basic geodetic mapping, and airborne surveys for satellite validation. He is the Danish Chairman for the Scientific Commission on Antarctic Research and a member of the ESA Advisory Board for Earth Observation.